

# Structurally Tailored Organic–Inorganic Perovskites: Optical Properties and Solution-Processed Channel Materials for Thin-Film Transistors

David B. Mitzi,\* Christos D. Dimitrakopoulos, and Laura L. Kosbar

IBM T. J. Watson Research Center, P.O. Box 218, Yorktown Heights, New York 10598

Received January 31, 2001. Revised Manuscript Received April 24, 2001

The structures, optical properties, and field-effect mobilities of three semiconducting *m*-fluorophenethylammonium-based  $(C_6H_4FC_2H_4NH_3)_2SnI_4$  perovskites ( $m = 2, 3, \text{ or } 4$ ) are reported and compared with the analogous measurements for the nonfluorosubstituted phenethylammonium system,  $(C_6H_5C_2H_4NH_3)_2SnI_4$ . The (4-fluorophenethylammonium) $_2$  $SnI_4$  system adopts a fully ordered monoclinic ( $P2_1/c$ ) cell with the lattice parameters  $a = 16.653(2)$  Å,  $b = 8.6049(8)$  Å,  $c = 8.7551(8)$  Å,  $\beta = 98.644(2)^\circ$ , and  $Z = 2$ . Both (3-fluorophenethylammonium) $_2$  $SnI_4$  and (2-fluorophenethylammonium) $_2$  $SnI_4$  are refined in a monoclinic ( $C2/c$ ) subcell with the lattice parameters  $a = 34.593(4)$  Å,  $b = 6.0990(8)$  Å,  $c = 12.254(2)$  Å,  $\beta = 103.917(2)^\circ$ , and  $Z = 4$  and  $a = 35.070(3)$  Å,  $b = 6.1165(5)$  Å,  $c = 12.280(1)$  Å,  $\beta = 108.175(1)^\circ$ , and  $Z = 4$ , respectively. Each hybrid structure consists of sheets of corner-sharing distorted  $SnI_6$  octahedra separated by bilayers of fluorophenethylammonium cations. The dominant low energy feature in the optical absorption spectra for spin-coated films of the new hybrids (an exciton band associated with the tin(II) iodide framework) shifts from 609 to 599 nm and 588 nm across the series  $m = 4$  to 2 (the corresponding value for the phenethylammonium-based system is 609 nm). This shift in optical properties is primarily attributed to subtle structural modifications induced by the organic cation substitutions, including a progressive shift in Sn–I–Sn tilt angle between adjacent  $SnI_6$  octahedra from  $156.375(8)^\circ$  for the  $m = 4$  structure to  $154.16(3)^\circ$  and  $153.28(3)^\circ$  (average) for the  $m = 3$  and 2 structures, respectively. The corresponding angle in the previously reported phenethylammonium-based structure is  $156.48^\circ$  (average), very similar to the  $m = 4$  value. Other potentially important structural modifications include the average Sn–I bond length and the degree of interaction between the substituted fluorine and the inorganic sheet. Saturation regime field-effect mobilities for thin-film field-effect transistors based on the new fluorophenethylammonium-based hybrids are similar to that previously observed in (phenethylammonium) $_2$  $SnI_4$ , typically ranging from  $\sim 0.2$  to  $0.6$   $cm^2 V^{-1} s^{-1}$ , with the maximum currents in the devices decreasing across the series  $m = 4$  to 2. The differences in transport properties can be attributed to the change in electronic structure, as well as to film morphology modification, brought about by the organic cation substitutions.

## Introduction

Organic–inorganic hybrids combine useful attributes of organic and inorganic materials within a single molecular scale composite, providing exciting opportunities for fundamental studies<sup>1,2</sup> as well as for the creation of organic–inorganic electronic technologies.<sup>3</sup> Crystalline composites are particularly interesting because of the ease with which the structural characteristics of the hybrids can be correlated with physical properties. The organic–inorganic perovskites are one important hybrid family, exhibiting a number of interesting magnetic, optical, and electrical phenomena as a result of the integration of organic and inorganic constituents, as

well as the possibility of processing the materials using low-temperature techniques.<sup>2,3</sup> Electroluminescence from a dye-containing perovskite, for example, which combines the thermal/mechanical stability and band gap tunability of an inorganic framework with the desirable luminescence properties of an organic component, has recently been reported.<sup>4</sup> An organic–inorganic thin-film transistor (TFT) has also been demonstrated, employing a  $(C_6H_5C_2H_4NH_3)_2SnI_4$  perovskite as the channel layer.<sup>5,6</sup> In these devices, the organic–inorganic hybrid enables the integration of simple processing (self-assembly) associated with organic materials and the higher carrier mobilities of inorganic compounds. Hybrid TFT devices based on the tin(II) iodide framework have been re-

\* To whom correspondence should be addressed.

(1) For a recent review, see: Papavassiliou, G. C. *Prog. Solid State Chem.* **1997**, 25, 125.

(2) For a recent review, see: Mitzi, D. B. *Prog. Inorg. Chem.* **1999**, 48, 1.

(3) Mitzi, D. B.; Chondroudis, K.; Kagan, C. R. *IBM J. Res. Dev.* **2001**, 45, 29.

(4) Chondroudis, K.; Mitzi, D. B. *Chem. Mater.* **1999**, 11, 3028.

(5) (a) Chondroudis, K.; Dimitrakopoulos, C. D.; Mitzi, D. B.; Unpublished work 1998. (b) Chondroudis, K.; Dimitrakopoulos, C. D.; Kagan, C. R.; Kymissis, I.; Mitzi, D. B. U.S. Patent US6,180,956, January 30, 2001.

(6) Kagan, C. R.; Mitzi, D. B.; Dimitrakopoulos, C. D. *Science* **1999**, 286, 945.

ported with mobilities ( $\sim 0.6 \text{ cm}^2 \text{ V}^{-1} \text{ s}^{-1}$ ) comparable to that of amorphous silicon (a-Si) with, however, the ability to solution process the channel layer at near-ambient temperatures.<sup>6</sup>

The high mobilities and semiconductor–metal transition observed in the  $(\text{RNH}_3)_2(\text{CH}_3\text{NH}_3)_{n-1}\text{Sn}_n\text{I}_{3n+1}$  perovskite family<sup>7</sup> are unusual among metal halides, which are more typically insulators. Each member consists of  $n$ -layer thick sheets of corner-sharing  $\text{SnI}_6$  octahedra (cut from the three-dimensional  $\text{CH}_3\text{NH}_3\text{SnI}_3$  perovskite structure), alternating with bilayers of  $\text{RNH}_3^+$  cations. The  $n = 1$  materials are semiconducting and are the first materials to have been incorporated into hybrid TFT devices. As  $n$  increases, the compounds become dramatically more conducting. The  $n \rightarrow \infty$  compound,  $\text{CH}_3\text{NH}_3\text{SnI}_3$ , is a low-carrier-density p-type metal with a carrier density of approximately  $10^{19}$  carriers/cm<sup>3</sup> and a Hall mobility of  $50\text{--}100 \text{ cm}^2 \text{ V}^{-1} \text{ s}^{-1}$ .<sup>8</sup> The band gap of the material appears to correlate with the degree of distortion of the  $\text{SnI}_6$  octahedra making up the sheets, as well as the average Sn–I bond length in the material. Namely, as the average Sn–I bond length and the degree of distortion decreases, the conductivity of the material increases (i.e., the band gap decreases).

Recently, the templating influence of the inorganic framework on the conformation and orientation of the organic cations in the hybrid structures has been discussed.<sup>9</sup> In the  $(\text{PEA})_2\text{MX}_4$  [PEA = phenethylammonium; M = divalent metal; X = halogen] compounds, for example, the conformation of the organic cation can be changed as a function of the metal halide framework.<sup>9,10</sup> The inorganic framework can also be used to control the orientation of photoreactive organic monomers, thereby selectively rendering them susceptible to polymerization under UV exposure.<sup>11,12</sup> Just as the inorganic framework can affect the structural character of the organic component of the hybrid, the organic cations can also influence the development and structure of the inorganic framework. In organic–inorganic perovskites of the form  $(\text{H}_2\text{AEQT})\text{M}_{2/3}\text{X}_4$  [AEQT = 5,5''-bis(aminoethyl)-2,2':5',2'':5'',2'''-quaterthiophene; M = trivalent metal; X = halogen], for example, the particularly stable layers of rigid, rodlike quaterthiophene moieties template the formation of metal-deficient inorganic sheets of corner-sharing metal halide octahedra.<sup>13</sup>

In this study, we seek to use the steric constraints and hydrogen-bonding interactions of different organic cation layers to influence the detailed bonding of the  $n = 1$  tin(II) iodide framework and therefore, presumably, the electronic properties of the material. Because the PEA cation has provided the highest mobilities to date for the hybrid TFT devices, this cation forms the starting point for the study. A functional group (in this case a fluorine atom) is substituted on the phenyl ring to influence both the structural character of the inor-

ganic framework as well as potentially the film formation characteristics of the hybrid. As the position of the fluorine atom is shifted among the 2, 3, and 4 positions on the phenyl ring, it is expected that the steric constraints and chemical interactions imposed by the substituted fluorine atom will produce subtle changes in the crystal and electronic structure of the materials.

## Experimental Section

**Synthesis.** *(4-fluorophenethylammonium)<sub>2</sub>SnI<sub>4</sub>* [(4-FPEA)<sub>2</sub>SnI<sub>4</sub>]. (4-FPEA)<sub>2</sub>SnI<sub>4</sub> crystals were grown from a slowly cooled, 2-butanol/hydriodic acid solution containing the organic and inorganic salts. First, 1.118 g (3 mmol) of  $\text{SnI}_2$  (Aldrich, anhydrous beads, 99.999%) was added to a test tube under an inert atmosphere, along with 10 mL of anhydrous 2-butanol, which was added through a syringe. After adding 0.79 mL (0.835 g; 6 mmol) of 4-fluorophenethylamine (Aldrich, 99%), the tube was cooled to  $-5 \text{ }^\circ\text{C}$  and 2 mL of concentrated (57 wt %) aqueous hydriodic acid was slowly added. The tube contents were thoroughly mixed and then heated to  $94 \text{ }^\circ\text{C}$ , leading to the complete dissolution of the  $\text{SnI}_2$  beads. The nominally saturated solution was cooled at  $3 \text{ }^\circ\text{C/h}$  to  $0 \text{ }^\circ\text{C}$ , yielding 2.55 g (93% theoretical yield) of dark red, thin (4-FPEA)<sub>2</sub>SnI<sub>4</sub> crystals. The crystals were filtered in an inert atmosphere and recrystallized twice from a mixture of anhydrous methanol and toluene. After drying under vacuum, the crystals were stored in an argon-filled glovebox with oxygen and water levels maintained below 1 ppm. Chemical analysis of the 4-fluorophenethylammonium ( $\text{C}_{16}\text{H}_{22}\text{F}_2\text{N}_2$ )<sub>2</sub>SnI<sub>4</sub> material yielded the following: Calcd [C (21.20%), H (2.45%), N (3.09%), F (4.19%)]; Found [C (21.12%), H (2.49%), N (3.07%), F (3.90%)].

Although the above materials were used to deposit thin films for optical and electrical measurements, thicker and better-formed crystals resulted from a slowly cooled concentrated hydriodic acid solution (i.e., with no 2-butanol) containing stoichiometric quantities of the organic and inorganic salts. These thicker crystals were used for single-crystal diffraction. Note that the powder X-ray diffraction patterns were identical for the materials produced using the two techniques (although the materials produced using pure hydriodic acid as solvent sometimes had a minor impurity phase of the 4-fluorophenethylammonium iodide salt).

*(3-fluorophenethylammonium)<sub>2</sub>SnI<sub>4</sub>* [(3-FPEA)<sub>2</sub>SnI<sub>4</sub>]. (3-FPEA)<sub>2</sub>SnI<sub>4</sub> crystals were grown using essentially an identical process to that described above for the 4-fluorophenethylammonium analogue. However, as the position of the fluorine is altered on the phenyl ring, the solubility of the organic cation and final product changes, and therefore, the amounts of the solvents were varied for the different organic cations in order to improve the yield. First, 1.118 g (3 mmol) of  $\text{SnI}_2$  (Aldrich, anhydrous beads, 99.999%) was placed in a sealed test tube under an inert atmosphere and 6 mL of anhydrous 2-butanol was added through a syringe. After adding 0.78 mL (0.835 g; 6 mmol) of 3-fluorophenethylamine (Aldrich, 99%), the tube was cooled to  $-5 \text{ }^\circ\text{C}$  and 1 mL of concentrated (57 wt %) aqueous hydriodic acid was slowly added. The mixture was heated to  $94 \text{ }^\circ\text{C}$  to dissolve the organic and inorganic salts and slow-cooled like for the 4-FPEA analogue, producing a large yield (2.5 g; 92% theoretical yield) of dark red, thin (3-FPEA)<sub>2</sub>SnI<sub>4</sub> crystals. The crystals were recrystallized and handled like for the 4-FPEA compound. Chemical analysis of the 3-fluorophenethylammonium ( $\text{C}_{16}\text{H}_{22}\text{F}_2\text{N}_2$ )<sub>2</sub>SnI<sub>4</sub> material yielded the following: Calcd [C (21.20%), H (2.45%), N (3.09%), F (4.19%)]; Found [C (21.19%), H (2.49%), N (3.11%), F (4.02%)].

Like for the (4-FPEA)<sub>2</sub>SnI<sub>4</sub> crystals, thicker and better-formed crystals resulted from a slowly cooled concentrated hydriodic acid solution containing stoichiometric quantities of the organic and inorganic salts. These thicker crystals were used for single-crystal diffraction.

*(2-fluorophenethylammonium)<sub>2</sub>SnI<sub>4</sub>* [(2-FPEA)<sub>2</sub>SnI<sub>4</sub>]. The (2-FPEA)<sub>2</sub>SnI<sub>4</sub> crystals were grown using exactly the same

(7) Mitzi, D. B.; Feild, C. A.; Harrison, W. T. A.; Guloy, A. M. *Nature* **1994**, *369*, 467.

(8) (a) Mitzi, D. B.; Feild, C. A.; Schlesinger, Z.; Laibowitz, R. B. *J. Solid State Chem.* **1995**, *114*, 159. (b) Mitzi, D. B.; Liang, K. *J. Solid State Chem.* **1997**, *134*, 376.

(9) Mitzi, D. B. *J. Chem. Soc., Dalton Trans.* **2001**, 1.

(10) Mitzi, D. B. *J. Solid State Chem.* **1999**, *145*, 694.

(11) Tieke, B.; Chapuis, G. *Mol. Cryst. Liq. Cryst.* **1986**, *137*, 101.

(12) Day, P.; Ledsham, R. D. *Mol. Cryst. Liq. Cryst.* **1982**, *86*, 163.

(13) Mitzi, D. B. *Inorg. Chem.* **2000**, *39*, 6107.

**Table 1. Crystallographic Data for (*m*-Fluorophenethylammonium)<sub>2</sub>SnI<sub>4</sub>, where *m* = 2, 3, and 4**

chemical formula	C <sub>16</sub> H <sub>22</sub> N <sub>2</sub> F <sub>2</sub> SnI <sub>4</sub> ( <i>m</i> = 4)	C <sub>16</sub> H <sub>22</sub> N <sub>2</sub> F <sub>2</sub> SnI <sub>4</sub> ( <i>m</i> = 3)	C <sub>16</sub> H <sub>22</sub> N <sub>2</sub> F <sub>2</sub> SnI <sub>4</sub> ( <i>m</i> = 2)
formula weight	906.69	906.69	906.69
space group	<i>P</i> 2 <sub>1</sub> / <i>c</i> (No. 14)	<i>C</i> 2/ <i>c</i> (No. 15)	<i>C</i> 2/ <i>c</i> (No. 15)
<i>a</i> , Å	16.653(2)	34.593(4)	35.070(3)
<i>b</i> , Å	8.6049(8)	6.0990(8)	6.1165(5)
<i>c</i> , Å	8.7551(8)	12.254(2)	12.280(1)
$\beta$ , deg	98.644(2)	103.917(2)	108.175(1)
<i>V</i> , Å <sup>3</sup>	1240.4(2)	2509.4(5)	2502.7(6)
<i>Z</i>	2	4	4
$\rho_{\text{calcd}}$ , g/cm <sup>3</sup>	2.428	2.400	2.406
wavelength (Å)	0.71073 (MoK $\alpha$ )	0.71073 (MoK $\alpha$ )	0.71073 (MoK $\alpha$ )
absorption coefficient ( $\mu$ ), cm <sup>-1</sup>	60.28	59.59	59.75
<i>R</i> <sub>i</sub> <sup>a</sup>	0.026	0.037	0.038
<i>R</i> <sub>w</sub> <sup>b</sup>	0.035	0.043	0.058
goodness of fit (GoF) <sup>c</sup>	1.66	1.88	2.51

<sup>a</sup>  $R_i = \sum(|F_o| - |F_c|)/\sum(|F_o|)$ . <sup>b</sup>  $R_w = \{\sum w(|F_o| - |F_c|)^2/\sum w|F_o|^2\}^{1/2}$ . <sup>c</sup>  $\text{GoF} = \{\sum w(|F_o| - |F_c|)^2/(n - m)\}^{1/2}$ , where *n* = number of reflections and *m* = number of refinement parameters.

process as that for the 3-fluorophenethylammonium analogue, yielding 2.0 g (74% theoretical yield) of the lighter red crystals. The crystals were recrystallized and handled as that for the other two analogues. Chemical analysis of the 2-fluorophenethylammonium (C<sub>16</sub>H<sub>22</sub>N<sub>2</sub>F<sub>2</sub>)SnI<sub>4</sub> material yielded the following: Calcd [C (21.20%), H (2.45%), N (3.09%), F (4.19%)]; Found [C (21.48%), H (2.47%), N (3.13%), F (4.16%)].

The above (2-FPEA)<sub>2</sub>SnI<sub>4</sub> materials were used to deposit thin films for optical and electrical measurements. Thicker and better-formed crystals for X-ray diffraction resulted from slow evaporation of an ethanol/toluene solution of the hybrid material.

**Thin Film Deposition.** Films of the three fluorophenethylammonium tin(II) iodide compounds, as well as the PEA-based analogue, were prepared in a nitrogen-filled drybox by spin-coating from solution. The quartz substrates for optical measurements were cleaned in aqua regia, followed by sonication in toluene (20 min), acetone (20 min), and methanol (20 min). They were subsequently placed in a 110 °C oven to dry. Silicon substrates for the electrical measurements were cleaned in water, followed by a methanol rinse, sonication in chloroform for 10 min, and oxygen plasma cleaning for 10 min. The spinning solution for each compound was prepared by dissolving 20 mg of the recrystallized hybrid in 1.6 mL of freshly dried and distilled methanol. The films were prepared by flooding the surface of the substrate with solution (filtered through a 0.2  $\mu$ m poly(tetrafluoroethylene) filter) and then initiating a spinning cycle (1 s ramp to 3000 rpm; dwell 30 s at 3000 rpm). Each substrate was annealed at 70 °C for 15 min after spinning to remove residual solvent. The films exhibited well-defined X-ray diffraction peaks corresponding to the (2*h* 0 0) series of reflections, indicating that the films were well crystallized and highly oriented. Examination of the films using atomic force microscopy (AFM) in tapping mode indicated that the films for the three new compounds were similar in nature, with, however, a tendency for significantly smaller grain size in the 2-FPEA system (feature size generally  $\leq$ 100 nm), compared with those of the 3-FPEA and 4-FPEA systems (grain size  $\sim$ 150–250 nm). Grain sizes in the (PEA)<sub>2</sub>SnI<sub>4</sub> films were typically intermediate compared to those of the two sets of fluorophenethylammonium systems. The films were approximately 20(3) nm thick, as measured using an AFM scan across a scratch in the film, created using a razor blade.

**X-ray Crystallography.** A red (4-FPEA)<sub>2</sub>SnI<sub>4</sub> [(3-FPEA)<sub>2</sub>SnI<sub>4</sub>/(2-FPEA)<sub>2</sub>SnI<sub>4</sub>] platelike crystal, with the approximate dimensions 0.03 mm  $\times$  0.28 mm  $\times$  0.70 mm [ $<$ 0.01 mm  $\times$  0.14 mm  $\times$  0.60 mm/0.02 mm  $\times$  0.40 mm  $\times$  0.54 mm], was selected under a microscope and attached to the end of a quartz fiber with 5 min epoxy. A full sphere of data was collected at room temperature on a Bruker SMART CCD diffractometer, equipped with a normal focus 2.4 kW sealed tube X-ray source (MoK $\alpha$  radiation). Intensity data were collected with a detector distance of approximately 5.0 cm, in 2272 frames with increas-

ing  $\omega$ , and an exposure time of 30 s [40 s/50 s] per frame. The increment in  $\omega$  between each frame was 0.3°. The initial monoclinic unit cell was selected for each compound on the basis of an indexing of 860 [350/350] reflections. The final unit cell parameters and crystal orientation matrix were obtained by a least-squares fit of 4833 [4440/5566] reflections. Note that for the (3-FPEA)<sub>2</sub>SnI<sub>4</sub> and (2-FPEA)<sub>2</sub>SnI<sub>4</sub> compounds examination of the CCD frames indicated the existence of two types of reflections. One set consisted of sharp, strong, well-defined peaks arising from a subcell with the lattice parameters *a* = 34.593(4) Å, *b* = 6.0990(8) Å, *c* = 12.254(2) Å,  $\beta$  = 103.917(2)°, and *Z* = 4 and *a* = 35.070(3) Å, *b* = 6.1165(5) Å, *c* = 12.280(1) Å,  $\beta$  = 108.175(1)°, and *Z* = 4, respectively. The second set of spots corresponded to a superstructure, which doubled the cell along both the *a* and *b* axes. Although a number of these reflections are strong, the reflections exhibit broad or substantially split  $\omega$  scans, suggesting a poorly ordered superstructure, as has been previously noted for (H<sub>2</sub>-AEQT)PbBr<sub>4</sub>.<sup>14</sup> Consequently, the subcell structure is considered in this study.

An empirical absorption correction based on equivalent reflections was applied to the intensity data.<sup>15</sup> The structure was solved and refined using the NRCVAX 386 PC version program.<sup>16</sup> First, the Sn and I atoms were located using direct methods. The F, N, C, and H atoms were then located using successive Fourier difference maps. For (3-FPEA)<sub>2</sub>SnI<sub>4</sub> and (2-FPEA)<sub>2</sub>SnI<sub>4</sub>, the hydrogen atoms for the disordered carbons and nitrogens were placed at idealized positions. All heavy atoms (Sn, I, C, N, and F) were refined anisotropically. The minimum and maximum peaks in the final difference Fourier maps corresponded to  $-1.38$  and  $0.80$  e/Å<sup>3</sup> [ $-0.75$  and  $1.25$  e/Å<sup>3</sup> /  $-0.650$  and  $1.050$  e/Å<sup>3</sup>]. No additional symmetry was detected for any of the compounds using the MISSYM program.<sup>17</sup> Selected crystallographic results for the three compounds are summarized in Table 1. The atomic coordinates for (4-FPEA)<sub>2</sub>SnI<sub>4</sub>, (3-FPEA)<sub>2</sub>SnI<sub>4</sub>, and (2-FPEA)<sub>2</sub>SnI<sub>4</sub> are listed in Tables 2–4, respectively. Selected bond distances and angles are provided for each compound in Tables 5–7. A complete listing of crystallographic data, along with anisotropic displacement parameters for each compound, is given as Supporting Information.

**Optical Properties.** Absorption spectra were obtained at room temperature on spin-coated films (deposited on quartz disks) of each (C<sub>6</sub>H<sub>4</sub>FC<sub>2</sub>H<sub>4</sub>NH<sub>3</sub>)<sub>2</sub>SnI<sub>4</sub> compound, as well as the analogous PEA derivative, (C<sub>6</sub>H<sub>5</sub>C<sub>2</sub>H<sub>4</sub>NH<sub>3</sub>)<sub>2</sub>SnI<sub>4</sub>, using a Hewlett-Packard UV–vis 8543 spectrophotometer.

(14) Mitzi, D. B.; Chondroudis, K.; Kagan, C. R. *Inorg. Chem.* **1999**, *38*, 6246.

(15) Sheldrick, G. M. *SADABS*; Institut für Anorganische Chemie der Universität Göttingen: Göttingen, Germany, 1997.

(16) Gabe, E. J.; Le Page, Y.; Charland, J.-P.; Lee, F. L.; White, P. S. *J. Appl. Crystallogr.* **1989**, *22*, 384.

(17) Le Page, Y. *J. Appl. Crystallogr.* **1988**, *21*, 983.

**Table 2. Positional and Thermal Parameters<sup>a</sup> for (4-FPEA)<sub>2</sub>SnI<sub>4</sub>**

atom	<i>x</i>	<i>y</i>	<i>z</i>	<i>B</i> <sub>iso</sub> (Å <sup>2</sup> )
Sn	0.0	0.0	0.0	2.38(1)
I(1)	0.99841(1)	0.69704(2)	0.19800(2)	3.25(1)
I(2)	0.19284(1)	0.98225(3)	0.06860(2)	3.26(1)
N	0.1586(2)	0.9263(4)	0.4685(4)	3.5(1)
C(1)	0.1943(3)	0.0377(5)	0.5907(5)	4.1(2)
C(2)	0.2810(3)	0.9946(6)	0.6516(5)	4.6(2)
C(3)	0.3353(2)	0.9984(4)	0.5313(4)	3.7(2)
C(4)	0.3634(2)	0.8615(5)	0.4736(5)	4.2(2)
C(5)	0.4128(3)	0.8628(6)	0.3600(6)	5.0(2)
C(6)	0.4334(3)	0.0026(5)	0.3038(5)	4.7(2)
C(7)	0.4084(3)	0.1398(6)	0.3568(6)	4.8(2)
C(8)	0.3592(2)	0.1387(5)	0.4698(5)	4.2(2)
F	0.4819(2)	0.0050(4)	0.1924(4)	7.5(2)

<sup>a</sup> Hydrogen atom positions are listed in Table S2 (Supporting Information). Anisotropic thermal parameters are listed in Table S3.

**Table 3. Positional and Thermal Parameters<sup>a</sup> for (3-FPEA)<sub>2</sub>SnI<sub>4</sub>**

atom	<i>x</i>	<i>y</i>	<i>z</i>	<i>B</i> <sub>iso</sub> (Å <sup>2</sup> )
Sn	0.0	0.49158(8)	0.25	3.62(3)
I(1)	-0.09550(1)	0.49136(6)	0.19131(3)	3.73(2)
I(2) <sup>b</sup>	0.00044(3)	0.6145(1)	-0.00050(7)	3.18(3)
I(3) <sup>b</sup>	0.00004(2)	0.9920(1)	0.19257(7)	3.30(3)
N(1a) <sup>b</sup>	0.0787(3)	0.988(2)	0.1317(9)	3.9(5)
N(1b) <sup>b</sup>	0.0786(3)	0.818(2)	0.0544(8)	3.8(5)
C(1a) <sup>b</sup>	0.0944(8)	0.012(5)	0.034(2)	5(1)
C(1b) <sup>b</sup>	0.0974(1)	0.037(5)	0.070(3)	5(1)
C(2)	0.1387(3)	0.062(2)	0.0630(9)	5.6(4)
C(3)	0.1662(2)	0.911(1)	0.1418(6)	3.9(3)
C(4)	0.1778(2)	0.957(2)	0.2564(7)	5.0(4)
C(5)	0.2016(3)	0.818(2)	0.3256(8)	6.3(5)
C(6)	0.2150(3)	0.629(2)	0.292(1)	7.1(6)
C(7)	0.2040(3)	0.580(2)	0.178(1)	7.2(6)
C(8)	0.1798(2)	0.719(1)	0.1047(8)	5.4(4)
F	0.2126(2)	0.864(1)	0.4371(5)	12.0(4)

<sup>a</sup> Hydrogen atom positions are listed in Table S4 (Supporting Information). Anisotropic thermal parameters are listed in Table S5. <sup>b</sup> Occupancy = 1/2.

**Table 4. Positional and Thermal Parameters<sup>a</sup> for (2-FPEA)<sub>2</sub>SnI<sub>4</sub>**

atom	<i>x</i>	<i>y</i>	<i>z</i>	<i>B</i> <sub>iso</sub> (Å <sup>2</sup> )
Sn	0.0	0.49817(7)	0.25	3.20(3)
I(1)	-0.09536(1)	0.49861(5)	0.17103(4)	4.43(2)
I(2) <sup>b</sup>	-0.00036(2)	0.6194(1)	-0.00002(5)	3.60(3)
I(3) <sup>b</sup>	0.00008(2)	0.99642(9)	0.19098(7)	3.79(4)
N(1a) <sup>b</sup>	0.0811(3)	0.991(2)	0.152(1)	4.1(5)
N(1b) <sup>b</sup>	0.0835(4)	0.842(3)	0.076(1)	7.9(8)
C(1a) <sup>b</sup>	0.099(1)	0.004(6)	0.064(2)	5(1)
C(1b) <sup>b</sup>	0.100(2)	0.052(8)	0.099(3)	9(2)
C(2)	0.1433(2)	0.053(1)	0.1034(7)	6.2(4)
C(3)	0.1703(2)	0.886(1)	0.1789(6)	5.0(4)
C(4)	0.1810(3)	0.886(2)	0.2932(9)	7.1(5)
C(5)	0.2058(3)	0.727(2)	0.3663(8)	10.1(7)
C(6)	0.2171(4)	0.563(2)	0.304(2)	13(1)
C(7)	0.2072(5)	0.577(3)	0.189(2)	15(1)
C(8)	0.1830(2)	0.710(2)	0.1119(9)	10.5(6)
F	0.1683(3)	0.038(1)	0.3398(7)	13.1(5)

<sup>a</sup> Hydrogen atom positions are listed in Table S7 (Supporting Information). Anisotropic thermal parameters are listed in Table S8. <sup>b</sup> Occupancy = 1/2.

**Electrical Measurements.** Thin-film field-effect transistors (TFT) based on spin-coated channel layers of each (C<sub>6</sub>H<sub>4</sub>-FC<sub>2</sub>H<sub>4</sub>NH<sub>3</sub>)<sub>2</sub>SnI<sub>4</sub> compound, as well as the analogous PEA derivative, were tested using a Hewlett-Packard 4145B semiconductor analyzer. The organic–inorganic TFT (OITFT) device structure is identical to that previously described<sup>18</sup> for organic TFTs with, however, the vacuum-deposited organic channel material replaced with the spin-coated organic–inorganic hybrid. Specifically, the OITFT consists of a heavily *n*-doped silicon wafer as the gate, 5000 Å thick thermally

**Table 5. Selected Bond Distances (Å) and Angles (deg) for (4-FPEA)<sub>2</sub>SnI<sub>4</sub>**

Sn–I(1)	3.1330(3)	I(1) <sup>b</sup> –Sn–I(1) <sup>c</sup>	90.969(9)
Sn–I(1) <sup>b</sup>	3.1330(3)	I(1) <sup>b</sup> –Sn–I(1) <sup>d</sup>	89.031(9)
Sn–I(1) <sup>c</sup>	3.1377(3)	I(1) <sup>b</sup> –Sn–I(2)	92.992(6)
Sn–I(1) <sup>d</sup>	3.1377(3)	I(1) <sup>b</sup> –Sn–I(2) <sup>b</sup>	87.008(6)
Sn–I(2)	3.1809(4)	I(1) <sup>c</sup> –Sn–I(1) <sup>d</sup>	180
Sn–I(2) <sup>b</sup>	3.1809(4)	I(1) <sup>c</sup> –Sn–I(2)	89.224(6)
N–C(1)	1.492(5)	I(1) <sup>c</sup> –Sn–I(2) <sup>b</sup>	90.776(6)
C(1)–C(2)	1.509(7)	I(1) <sup>d</sup> –Sn–I(2)	90.776(6)
C(2)–C(3)	1.488(6)	I(1) <sup>d</sup> –Sn–I(2) <sup>b</sup>	89.224(6)
C(3)–C(4)	1.390(6)	I(2)–Sn–I(2) <sup>b</sup>	180
C(4)–C(5)	1.382(7)	N–C(1)–C(2)	110.6(4)
C(5)–C(6)	1.363(7)	C(1)–C(2)–C(3)	113.3(4)
C(6)–C(7)	1.358(7)	C(2)–C(3)–C(4)	120.8(4)
C(7)–C(8)	1.376(7)	C(2)–C(3)–C(8)	121.9(4)
C(8)–C(3)	1.404(6)	C(3)–C(4)–C(5)	121.6(4)
		C(4)–C(5)–C(6)	118.5(4)
C(6)–F	1.356(5)	C(5)–C(6)–C(7)	122.5(4)
I(1)–Sn–I(1) <sup>b</sup>	180	C(6)–C(7)–C(8)	119.1(4)
I(1)–Sn–I(1) <sup>c</sup>	89.031(9)	C(7)–C(8)–C(3)	121.0(4)
I(1)–Sn–I(1) <sup>d</sup>	90.969(9)	C(8)–C(3)–C(4)	117.3(4)
I(1)–Sn–I(2)	87.008(6)	F–C(6)–C(7)	118.6(4)
I(1)–Sn–I(2) <sup>b</sup>	92.992(6)	F–C(6)–C(5)	118.9(4)
		Sn–I(1)–Sn <sup>a</sup>	156.375(8)

<sup>a</sup> 2 – *x*, –0.5 + *y*, 0.5 – *z*. <sup>b</sup> 2 – *x*, 2 – *y*, –*z*. <sup>c</sup> 2 – *x*, 0.5 + *y*, 0.5 – *z*. <sup>d</sup> *x*, 1.5 – *y*, –0.5 + *z*.

**Table 6. Selected Bond Distances (Å) and Angles (deg) for (3-FPEA)<sub>2</sub>SnI<sub>4</sub>**

Sn–I(1)	3.2074(6)	I(1) <sup>a</sup> –Sn–I(2) <sup>b</sup>	88.95(2)
Sn–I(1) <sup>a</sup>	3.2074(6)	I(1) <sup>a</sup> –Sn–I(3)	89.70(2)
Sn–I(2) <sup>a</sup>	3.1634(9)	I(1) <sup>a</sup> –Sn–I(3) <sup>c</sup>	90.31(2)
Sn–I(2) <sup>b</sup>	3.1215(9)	I(2) <sup>a</sup> –Sn–I(3)	89.28(2)
Sn–I(3)	3.1321(9)	I(2) <sup>a</sup> –Sn–I(3) <sup>c</sup>	90.70(2)
Sn–I(3) <sup>c</sup>	3.1273(9)	I(2) <sup>b</sup> –Sn–I(2) <sup>a</sup>	178.17(3)
I(1)–Sn–I(1) <sup>a</sup>	179.96(2)	I(2) <sup>b</sup> –Sn–I(3)	88.97(2)
I(1)–Sn–I(2) <sup>a</sup>	88.43(2)	I(2) <sup>b</sup> –Sn–I(3) <sup>c</sup>	91.05(2)
I(1)–Sn–I(2) <sup>b</sup>	91.04(2)	I(3)–Sn–I(3) <sup>c</sup>	179.98(2)
I(1)–Sn–I(3)	90.35(2)	Sn <sup>d</sup> –I(3)–Sn	154.00(3)
I(1)–Sn–I(3) <sup>c</sup>	89.65(2)	Sn–I(2) <sup>a</sup> –Sn <sup>e</sup>	154.32(3)
I(1) <sup>a</sup> –Sn–I(2) <sup>a</sup>	91.58(2)		

<sup>a</sup> –*x*, *y*, 0.5 – *z*. <sup>b</sup> –*x*, 1 – *y*, –*z*. <sup>c</sup> –*x*, –1 + *y*, 0.5 – *z*. <sup>d</sup> *x*, 1 + *y*, *z*. <sup>e</sup> *x*, 1 – *y*, 1 – *z*.

**Table 7. Selected Bond Distances (Å) and Angles (deg) for (2-FPEA)<sub>2</sub>SnI<sub>4</sub>**

Sn–I(1)	3.1782(5)	I(1) <sup>a</sup> –Sn–I(2) <sup>b</sup>	88.51(2)
Sn–I(1) <sup>a</sup>	3.1782(5)	I(1) <sup>a</sup> –Sn–I(3)	89.60(2)
Sn–I(2) <sup>a</sup>	3.1547(6)	I(1) <sup>a</sup> –Sn–I(3) <sup>c</sup>	90.40(2)
Sn–I(2) <sup>b</sup>	3.1568(6)	I(2) <sup>a</sup> –Sn–I(3)	89.80(2)
Sn–I(3)	3.1327(7)	I(2) <sup>a</sup> –Sn–I(3) <sup>c</sup>	90.29(2)
Sn–I(3) <sup>c</sup>	3.1535(7)	I(2) <sup>b</sup> –Sn–I(2) <sup>a</sup>	179.39(2)
I(1)–Sn–I(1) <sup>a</sup>	179.90(2)	I(2) <sup>b</sup> –Sn–I(3)	89.77(2)
I(1)–Sn–I(2) <sup>a</sup>	88.92(2)	I(2) <sup>b</sup> –Sn–I(3) <sup>c</sup>	90.14(2)
I(1)–Sn–I(2) <sup>b</sup>	91.52(2)	I(3)–Sn–I(3) <sup>c</sup>	179.91(2)
I(1)–Sn–I(3)	90.30(2)	Sn <sup>d</sup> –I(3)–Sn	153.31(3)
I(1)–Sn–I(3) <sup>c</sup>	89.70(2)	Sn–I(2) <sup>a</sup> –Sn <sup>e</sup>	153.24(3)
I(1) <sup>a</sup> –Sn–I(2) <sup>a</sup>	91.06(2)		

<sup>a</sup> –*x*, *y*, 0.5 – *z*. <sup>b</sup> –*x*, 1 – *y*, –*z*. <sup>c</sup> –*x*, –1 + *y*, 0.5 – *z*. <sup>d</sup> *x*, 1 + *y*, *z*. <sup>e</sup> *x*, 1 – *y*, 1 – *z*.

grown oxide gate dielectric, Pd source and drain electrodes with a chromium adhesion layer (deposited by evaporation through a silicon membrane shadow mask<sup>18</sup>), and the spin-coated organic–inorganic hybrid channel material. The source and drain electrodes are deposited directly on the gate dielectric, followed by deposition of the hybrid material. The channel length (*L*), defined as the distance between the source and drain electrode, ranged from 5 to 95 μm, whereas the channel width (*W*) ranged from 250 to 1500 μm. The devices were isolated by removing excess hybrid film between adjacent devices using a methanol-soaked cotton swab and were

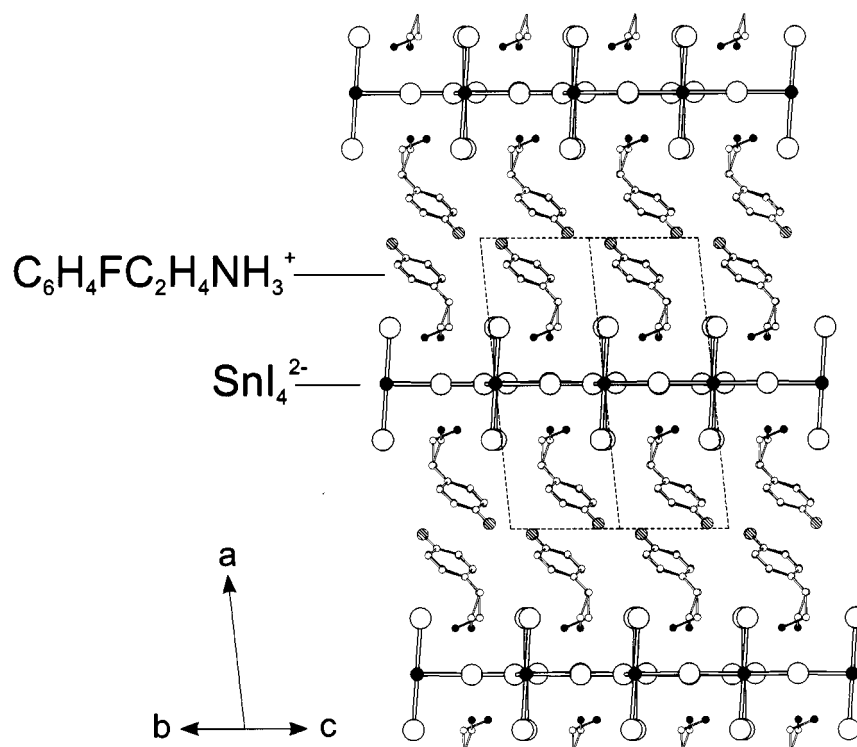


**Figure 1.** Crystal structure of  $(4\text{-FPEA})_2\text{SnI}_4$ , viewed approximately along the (011) axis. Dashed lines depict the unit cell outline. For clarity, the atoms are represented as spheres with uniform sizes selected for each atom type.

fabricated, maintained, and tested in a nitrogen-filled drybox with oxygen and water levels below 1 ppm.

### Results and Discussion

**Crystal Structures.** The basic building block of the  $(4\text{-FPEA})_2\text{SnI}_4$  structure consists of well-ordered anionic layers of corner-sharing  $\text{SnI}_6$  octahedra, with a layer of 4-fluorophenethylammonium cations capping each inorganic sheet on both sides (Figure 1). The organic cations are hydrogen-bonded to halogens in the inorganic sheet through the pendant ammonium group. The full three-dimensional structure is created by stacking the neutral organic-sheathed perovskite layers along the  $a$  axis. Weak (e.g., van der Waals) interactions between the fluorophenyl groups of successive  $(\text{C}_6\text{H}_4\text{FC}_2\text{H}_4\text{NH}_3)_2\text{-SnI}_4$  layers hold the structure together, with essentially no interleaving among the fluorophenethylammonium cations from adjacent layers. Fluorine atoms from adjacent layers weakly interact, with closest  $\text{F}\cdots\text{F}$  distances of 3.512(6) Å. These interlayer  $\text{F}\cdots\text{F}$  distances are significantly more than twice the van der Waals radius ( $\sim 1.47$  Å)<sup>19</sup> for fluorine. The interlayer  $\text{C}(5)\cdots\text{C}(7)'$  distance [3.577(6) Å] between phenyl rings, however, is approximately twice the van der Waals radius for aromatic carbon atoms ( $\sim 1.77$  Å).<sup>19</sup>

The monoclinic ( $P2_1/c$ ) unit cell for  $(4\text{-FPEA})_2\text{SnI}_4$  is analogous to that reported for  $(\text{CH}_3\text{NH}_3)_2\text{CuCl}_4$  (after permuting the  $a$  and  $c$  axes in the latter compound).<sup>20</sup> In each case, the dimensions of the monoclinic unit cell in the plane of the perovskite sheets are approximately  $\sqrt{2}a_p \times \sqrt{2}a_p$ , where  $a_p$  is the simple cubic perovskite lattice parameter [i.e.,  $a_p = 6.2397(5)$  Å for  $\text{CH}_3\text{NH}_3\text{-}$

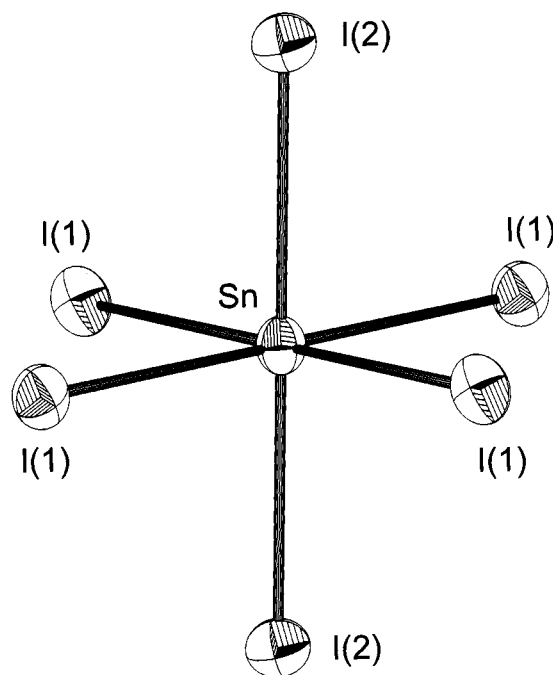


**Figure 2.** The  $\text{SnI}_6$  octahedra structure in  $(4\text{-FPEA})_2\text{SnI}_4$ , showing atom labeling and thermal ellipsoids for the Sn and I atoms. The thermal ellipsoids are drawn at 50% probability.

$\text{SnI}_3$ ].<sup>8</sup> The  $\sqrt{2} \times \sqrt{2}$  superstructure in the  $b$ - $c$  crystallographic plane arises from tilting and rotation of the  $\text{SnI}_6$  octahedra relative to each other, as well as from the ordering of the organic cations and is common among other organic-inorganic perovskites.<sup>2,10</sup> The inorganic sheets are derived from one crystallographically independent  $\text{SnI}_6$  octahedron (Figure 2), with shorter bridging  $\text{Sn-I}(1)$  bonds [3.1330(3) and 3.1377(3) Å] and longer 3.1809(4) Å apical  $\text{Sn-I}(2)$

(19) Bondi, A. *J. Phys. Chem.* **1964**, *68*, 441.

(20) Pabst, I.; Fuess, H.; Bats, J. W. *Acta Crystallogr.* **1987**, *C43*, 413.

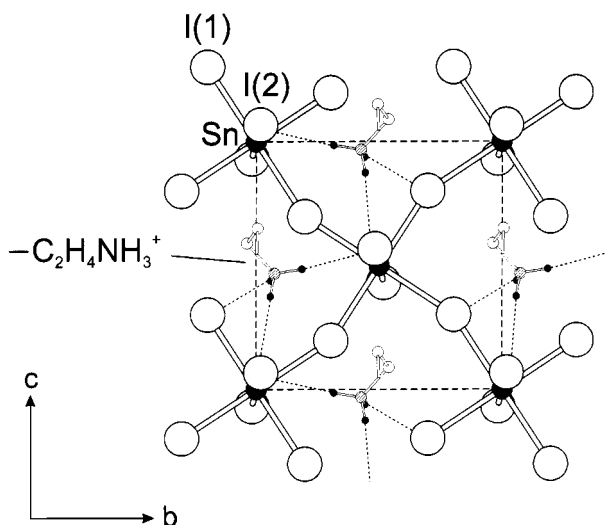


**Figure 3.** Single (4-FPEA)<sub>2</sub>SnI<sub>4</sub> layer, viewed perpendicular to the plane of the layer, showing the relative rotations of the SnI<sub>6</sub> octahedra in the plane of the sheet and the hydrogen bonding of the organic cation. For clarity, only the ethylammonium component of the 4-FPEA cation is shown and the organic cations on the bottom side of the layer have been removed from the figure. Similarly, only the hydrogen atoms associated with the nitrogens are depicted. The atoms are represented as spheres with uniform sizes selected for each atom type.

bonds (Table 5). The range of bond lengths is very similar to that reported<sup>21</sup> for orthorhombic (*Pbca*) (C<sub>4</sub>H<sub>9</sub>NH<sub>3</sub>)<sub>2</sub>SnI<sub>4</sub> [3.133(1) and 3.138(1) Å bridging bonds; 3.160(2) Å apical bonds], with an average Sn–I bond length of 3.151 Å. In addition to the bond length differences, the I–Sn–I bond angles (Table 5) deviate slightly from 90°, with the biggest difference [92.992(6)°] occurring for the I(1)–Sn–I(2) angle. The 156.375(8)° Sn–I(1)–Sn angle primarily reflects the relative rotations of the SnI<sub>6</sub> octahedra within each layer in the *b*–*c* plane (see Figure 3).

As a result of the geometric constraints of the ammonium group and the organic tail in organic–inorganic layered perovskite structures, the primary N–H⋯I hydrogen-bonding interactions are generally either with two terminal and one bridging halogen (terminal halogen configuration) or with two bridging and one terminal halogen (bridging halogen configuration).<sup>2,22</sup> The terminal halogen configuration is often adopted by systems with aromatic organic cations, as in (PEA)<sub>2</sub>PbCl<sub>4</sub>, because this geometry reduces the interaction between the aromatic moiety and the terminal halogens.<sup>10</sup> The related (PEA)<sub>2</sub>CuX<sub>4</sub> (X = Cl and Br) structures, however, adopt the bridging halogen hydrogen-bonding configuration,<sup>23</sup> as a result of the antiferrodistortive arrangement of the long semicoordinate Cu–X bonds in the plane of the perovskite sheets (resulting from the Jahn–Teller distortion of the CuX<sub>6</sub> octahedra). In (4-FPEA)<sub>2</sub>SnI<sub>4</sub>, the 4-fluorophenethylammonium cation adopts the more typical terminal hydrogen-bonding configuration (Figure 3), with hydrogen bonding (H⋯I) distances of 2.68(5) and 2.74(4) Å for the two terminal N–H⋯I interactions and 2.94(6) Å for the primary

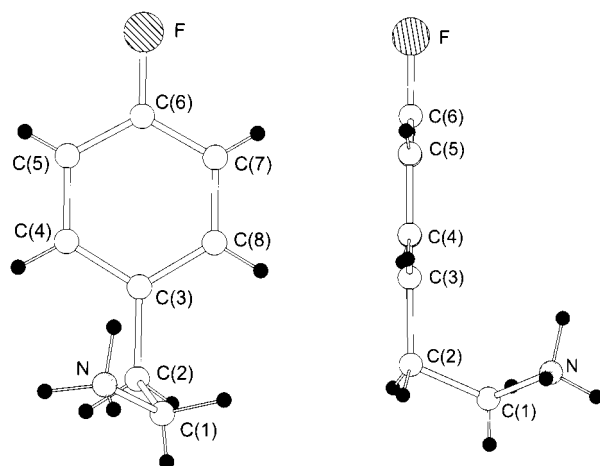


**Figure 4.** Front and side view of the 4-fluorophenethylammonium cation in (4-FPEA)<sub>2</sub>SnI<sub>4</sub>, showing atom labeling.

bridging N–H⋯I interaction. The J-shaped (or gauche) conformation of the 4-fluorophenethylammonium (Figure 4) is similar to that reported for the PEA cation in (PEA)<sub>2</sub>PbCl<sub>4</sub>.<sup>10</sup> Calculations for protonated phenethylamine and various substituted phenethylamines (including 4-fluorophenethylamine) indicate that the gauche conformation of the cation is substantially more stable than the anti conformation in the gas phase.<sup>24</sup> Apparently, in the current system, the solid-state interactions do not destabilize the gauche conformation [in contrast with the copper(II)-based (PEA)<sub>2</sub>CuX<sub>4</sub> systems, wherein the PEA cation adopts the anti conformation].<sup>23</sup>

The isostructural lattices of (3-FPEA)<sub>2</sub>SnI<sub>4</sub> and (2-FPEA)<sub>2</sub>SnI<sub>4</sub> (Figure 5) are similar to that discussed above for (4-FPEA)<sub>2</sub>SnI<sub>4</sub>. In (3-FPEA)<sub>2</sub>SnI<sub>4</sub> (Figure 5a), each tin(II) atom in the inorganic sheet is surrounded by a distorted octahedron of iodides, with bond lengths (Table 6) ranging from 3.1215(9) to 3.2074(6) Å [3.160 Å average]. The range of bond lengths and average bond length are slightly larger than the analogous values for the 4-FPEA perovskite. The I–Sn–I bond angles (Table 6) deviate slightly from 90°, with the biggest difference [88.43(2)°] occurring for the I(1)–Sn–I(2)<sup>a</sup> angle. Also, the bridging Sn–I–Sn bond angles are substantially different from 180° [i.e., 154.32(3) and 154.00(3)°], indicating that adjacent octahedra are substantially rotated relative to each other in the *b*–*c* plane. In isostructural (2-FPEA)<sub>2</sub>SnI<sub>4</sub> (Figure 5b), the bond lengths (Table 7) range from 3.1327(7) to 3.1782(5) Å [3.159 Å average], with nominally orthogonal bond angles ranging from 88.51(2) to 91.52(2)°. The bridging Sn–I–Sn angles are further rotated from 180° [153.24(3) and 153.31(3)°] compared with those of the 3-FPEA and 4-FPEA systems.

In contrast to the  $\sqrt{2}a_p \times \sqrt{2}a_p$  in-plane cell dimensions of the fully ordered (4-FPEA)<sub>2</sub>SnI<sub>4</sub> structure, the partially disordered monoclinic (*C2/c*) subcells for (3-FPEA)<sub>2</sub>SnI<sub>4</sub> and (2-FPEA)<sub>2</sub>SnI<sub>4</sub> are analogous to that observed in (H<sub>2</sub>AEQT)PbBr<sub>4</sub>,<sup>14</sup> with an *a*<sub>p</sub> × 2*a*<sub>p</sub> cell in the plane of the inorganic sheets. Both bridging iodides in the subcell model for the 3-FPEA and 2-FPEA compounds, I(2) and I(3), are refined as disordered over two symmetry-related sites (“a” and “b”), with an

(21) Mitzi, D. B. *Chem. Mater.* **1996**, *8*, 791.

(22) Chapuis, G.; Kind, R.; Arend, H. *Phys. Status Solidi A* **1976**, *36*, 285.

(23) Willett, R. D. *Acta Crystallogr.* **1990**, *C46*, 565.

(24) Urban, J. J.; Cronin, C. W.; Roberts, R. R.; Famini, G. R. *J. Am. Chem. Soc.* **1997**, *119*, 12292.

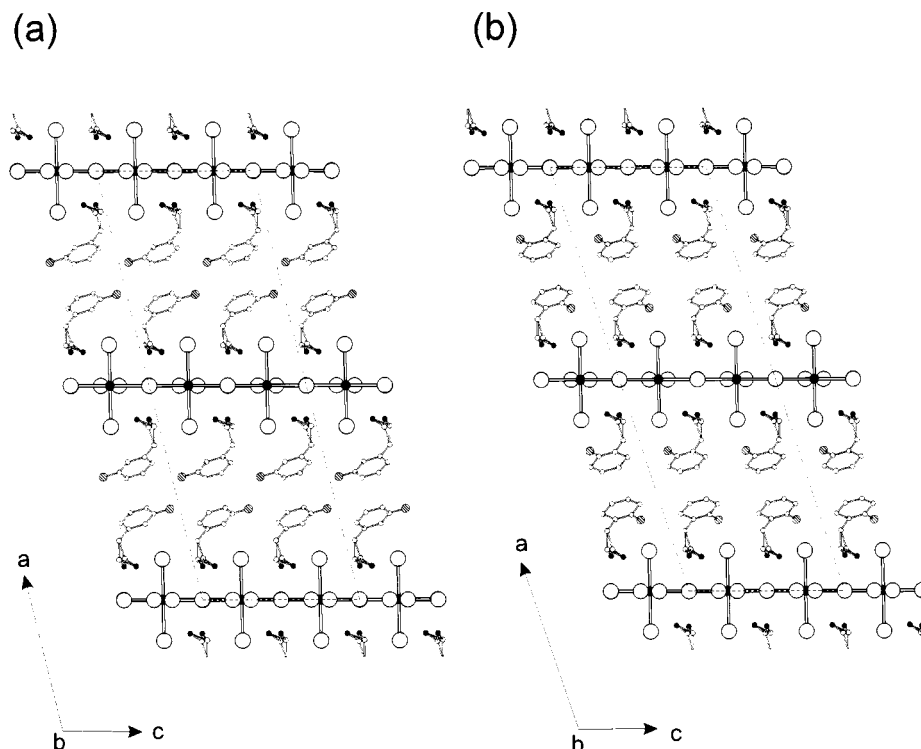


**Figure 5.** Crystal structures of (a)  $(3\text{-FPEA})_2\text{SnI}_4$  and (b)  $(2\text{-FPEA})_2\text{SnI}_4$ , viewed down the  $b$  axis. Dashed lines depict the unit cell outline. For clarity, the atoms are represented as spheres with uniform sizes selected for each atom type.

occupancy fixed at 0.5 [both the tin atom and the terminal iodides, I(1), are not disordered]. As is typically the case in the layered perovskites,<sup>2</sup> each organic cation sits nominally in a distorted square defined by four nearest neighbor tin(II) atoms and the Sn–I–Sn linkages between them (Figure 6). The square can be either “pinched-in” along the  $c$  axis and “pushed-out” along the  $b$  axis [Figure 6a] or “pushed-out” along the  $c$  axis and “pinched-in” along the  $b$  axis [Figure 6b]. A mixture of these two possibilities within a given square is unlikely [i.e., a square defined by either Sn, I(2a), or I(3b) or Sn, I(2b), or I(3a)] because this would lead to unreasonably short [3.304(1) or 3.359(1) Å] I⋯I contacts (note that  $2R_1 = 4.40$  Å, where  $R_1$  is the ionic radius for an  $\text{I}^-$  ion<sup>25</sup>).

The bridging iodides must therefore be distributed (with equal probability) between the two geometries described in Figure 6. Within a given sheet, the distortion of one square (defined by one set of four  $\text{SnI}_6$  octahedra) fixes the distortion for each nearest-neighbor square of octahedra (i.e., they must be in the opposite configuration). Consequently, as previously discussed for the  $(\text{H}_2\text{AEQT})_2\text{PbBr}_4$  structure,<sup>14</sup> each sheet must be nominally ordered and the apparent iodide disorder (or lack of a well-defined superstructure) can most reasonably be attributed to a loss of registry between adjacent perovskite sheets rather than from disorder within a given sheet. The poorly ordered superstructure, observed along the  $a$  and  $b$  axes in the X-ray data (not accounted for in the current subcell model), most likely relates to this incomplete ordering between sheets.

The 3-fluorophenethylammonium and 2-fluorophenethylammonium cations each adopt a similar J-shaped conformation to that discussed for  $(4\text{-FPEA})_2\text{SnI}_4$ . The fluorophenyl component of the cation is fully ordered

within each subcell model, whereas the ethylammonium tethering group is disordered over two different conformations (Figure 6). In both cases, the hydrogen bonding is accomplished in a terminal halogen hydrogen-bonding configuration, like that for the 4-FPEA analogue. The resulting ordering of the fluorophenyl moieties in  $(3\text{-FPEA})_2\text{SnI}_4$  and  $(2\text{-FPEA})_2\text{SnI}_4$  is substantially different than that encountered in the  $(4\text{-FPEA})_2\text{SnI}_4$  system (Figure 7). In the 4-FPEA system, the 4-fluorophenyl moieties pack in such a way that all of the phenyl rings in a given layer are parallel (Figure 7a). In the case of the 3-FPEA and 2-FPEA systems, the fluorophenyl moieties pack in a herringbone arrangement, as is commonly observed among aromatic systems (Figure 7b).<sup>13,26–29</sup> The prevalence of this packing arrangement can be understood in terms of edge-to-face (tilted-T) aromatic interactions between the organic moieties.<sup>30–33</sup>

Fluorine–fluorine distances between layers for the 3-FPEA system are 3.02(1) Å, very close to twice the van der Waals radius for fluorine and indicative of close contacts between the fluorines in the adjacent 3-FPEA layers. By contrast, the fluorine atoms are tucked away in the organic layers of  $(2\text{-FPEA})_2\text{SnI}_4$  and there are therefore no F⋯F distances closer than 6 Å. The closest interlayer interactions in this system include C(5)⋯C(5)′

(26) Brock, C. P.; Dunitz, J. D. *Acta Crystallogr.* **1982**, *B38*, 2218.

(27) Brock, C. P.; Dunitz, J. D. *Acta Crystallogr.* **1990**, *B46*, 795.

(28) Hargreaves, A.; Rizvi, S. *Acta Crystallogr.* **1962**, *15*, 365.

(29) Delugeard, Y.; Desuche, J.; Baudour, J. L. *Acta Crystallogr.* **1976**, *B32*, 702.

(30) Barclay, T. M.; Cordes, A. W.; MacKinnon, C. D.; Oakley, R. T.; Reed, R. W. *Chem. Mater.* **1997**, *9*, 981.

(31) Hunter, C. A.; Sanders, J. K. M. *J. Am. Chem. Soc.* **1990**, *112*, 5525.

(32) Paliwal, S.; Geib, S.; Wilcox, C. S. *J. Am. Chem. Soc.* **1994**, *116*, 4497.

(33) Jorgensen, W. L.; Severance, D. L. *J. Am. Chem. Soc.* **1990**, *112*, 4768.

(25) Shannon, R. D. *Acta Crystallogr.* **1976**, *A32*, 751.

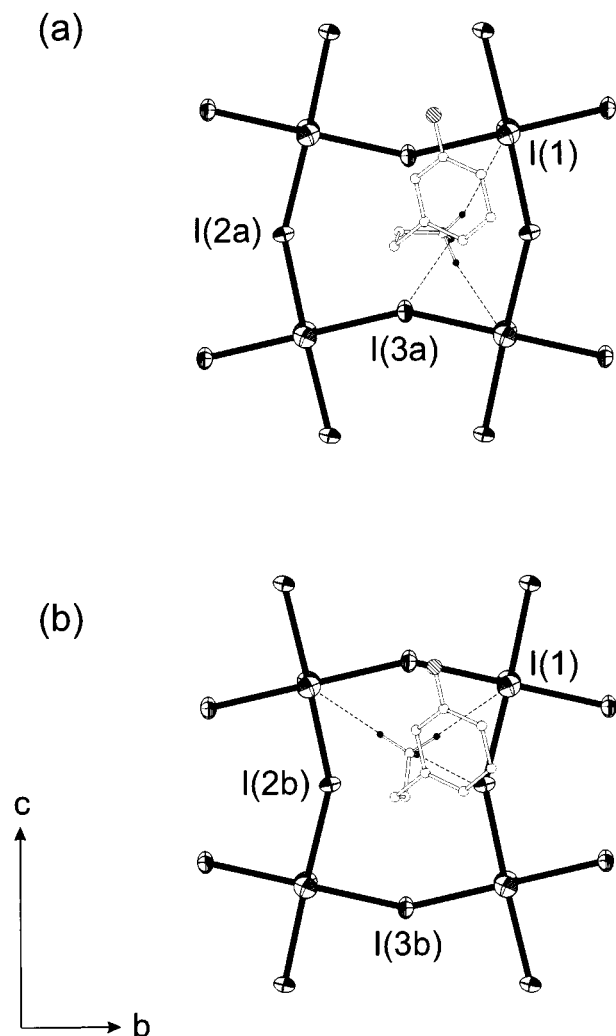


**Figure 6.** Two configurations for the tin(II) iodide framework and the 3-fluorophenethylammonium (3-FPEA) cation are shown in (a) and (b), along with atom labeling and thermal ellipsoids for the inorganic framework. The primary hydrogen-bonding interactions between the ammonium head of each 3-FPEA cation and the iodides in the inorganic sheet are indicated as dashed lines. The atoms in the organic cation are drawn as spheres with arbitrary size. The thermal ellipsoids for the inorganic framework are drawn at 50% probability.

[3.76(2) Å]. Furthermore, in contrast to the other two fluorophenethylammonium systems, in which there are no substantial interactions between the fluorine and iodides in the tin(II) iodide sheets, in (2-FPEA)<sub>2</sub>SnI<sub>4</sub>, the 3.782(8) Å F⋯I distance indicates a close interaction between the organic cation fluorine and the inorganic framework.

Finally, the new perovskites based on the various fluorophenethylammonium cations can be compared with the previously reported structure for (PEA)<sub>2</sub>SnI<sub>4</sub>.<sup>34</sup> The PEA compound has been refined in the monoclinic (*C2/m*) cell with the lattice parameters  $a = 32.640(1)$  Å,  $b = 6.117(3)$  Å,  $c = 6.164(3)$  Å, and  $\beta = 93.214(9)^\circ$ . The dimensions in the plane of the perovskite sheet are approximately  $a_p \times a_p$  with, however, disordering of both the in-plane iodides [as for the (3-FPEA)<sub>2</sub>SnI<sub>4</sub> and (2-FPEA)<sub>2</sub>SnI<sub>4</sub> structures] and the organic cations (including the phenyl rings). In fact, both the (3-FPEA)<sub>2</sub>SnI<sub>4</sub>

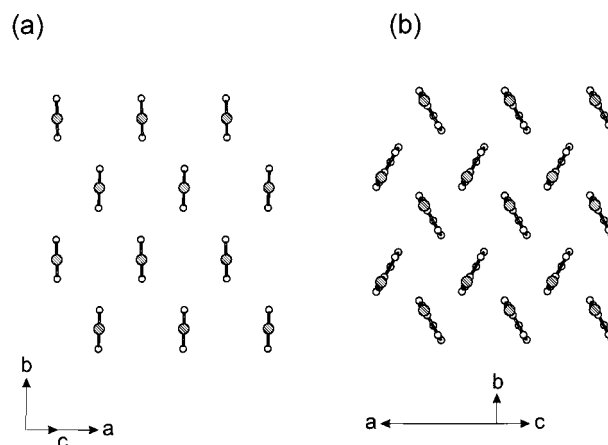


**Figure 7.** View parallel to the phenyl ring plane in a single layer of fluorophenethylammonium cations in (a) (4-FPEA)<sub>2</sub>SnI<sub>4</sub> and (b) (3-FPEA)<sub>2</sub>SnI<sub>4</sub>. For clarity, the ethylammonium tethering group for each cation and the tin(II) iodide component of the structure has been removed.

and (2-FPEA)<sub>2</sub>SnI<sub>4</sub> structures can be refined in the same  $a_p \times a_p$  cell with satisfactory refinement results. However, ultimately, the observation of superstructure peaks led us to adopt the larger  $a_p \times 2a_p$  cell (and the space group switch from *C2/m* to *C2/c*), which removed most of the disorder in the organic cation layer.

The inorganic framework for the (PEA)<sub>2</sub>SnI<sub>4</sub> structure is analogous to that in (3-FPEA)<sub>2</sub>SnI<sub>4</sub> and (2-FPEA)<sub>2</sub>SnI<sub>4</sub>, with Sn–I bond lengths ranging from 3.126 to 3.161 Å and an average bond length of 3.144 Å (smaller than any of the fluorophenethylammonium analogues).<sup>34,35</sup> The Sn–I–Sn bond angles are 156.74 and 156.23° for the two independent iodide linkages, very similar to the value observed in (4-FPEA)<sub>2</sub>SnI<sub>4</sub> [156.375(8)°] and larger than the angles observed in (3-FPEA)<sub>2</sub>SnI<sub>4</sub> [154.16(3)° average] and (2-FPEA)<sub>2</sub>SnI<sub>4</sub> [153.28(3)° average]. The shifts in Sn–I–Sn bond angle, average Sn–I bond length, and potentially the interaction between the fluorine substituted ring (where present) and the inorganic sheet are all expected to play a role in distinguishing the electronic structure of the hybrid.

**Film Morphology.** In addition to modifying the bulk electronic structure through crystal structure modification, substituting different organic cations can also influence film morphology (e.g., grain size and shape and crystallographic orientation) by modifying the degree of solubility and the underlying structure of the hybrid. Terminal groups on the cation can also be designed to have targeted interactions with the substrate, providing a further opportunity for control of film morphology. Note that for optical and especially electrical measurements the film morphology can be as important a parameter as crystal structure in determining the physical properties. Reducing the grain size can lead to quantum confinement effects,<sup>36</sup> whereas grain orientation, size, and connectivity can substantially influence transport properties in a polycrystalline film.

In the current (*m*-FPEA)<sub>2</sub>SnI<sub>4</sub> films (all deposited using the same solution concentration and spin speed), the  $m = 4$  and  $m = 3$  systems have a very similar grain

(34) Papavassiliou, G. C.; Koutselas, I. B.; Terzis, A.; Whangbo, M.-H. *Solid State Commun.* **1994**, *91*, 695.

(35) Koutselas, I. B. Private communication.  
(36) Chondroudis, K.; Mitzi, D. B.; Brock, P. *Chem. Mater.* **2000**, *12*, 169.

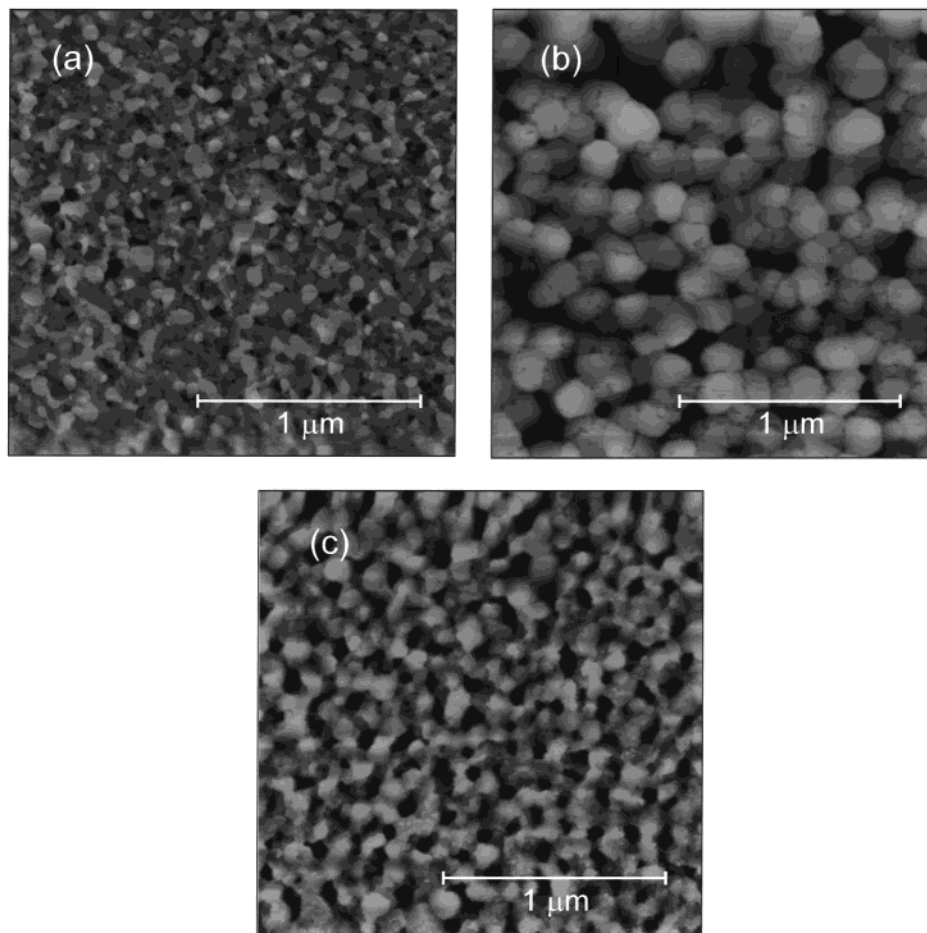


**Figure 8.** Atomic force microscope (AFM) topography images for spin-cast films of (a) (2-FPEA)<sub>2</sub>SnI<sub>4</sub>, (b) (3-FPEA)<sub>2</sub>SnI<sub>4</sub>, and (c) (PEA)<sub>2</sub>SnI<sub>4</sub> on silicon substrates with 5000 Å of thermally grown oxide. Each film was imaged within the channel region of a similar TFT device.

structure (grain size ~150–250 nm), whereas the  $m = 2$  films exhibit substantially smaller grain size (grain size  $\leq 100$  nm; Figure 8). The (PEA)<sub>2</sub>SnI<sub>4</sub> films, deposited using the same conditions, yield films with an intermediate grain size (Figure 8c) compared to the (2-FPEA)<sub>2</sub>SnI<sub>4</sub> and (3-FPEA)<sub>2</sub>SnI<sub>4</sub> films (Figure 8 parts a and b, respectively). The changes in film morphology might either arise from the different solubility of the organic cations as a function of the position of the fluorine substitution (2-FPEA is more soluble than 4-FPEA in many polar solvents) or from variations in the cation-substrate interactions (in this case, the fluorine atom should interact with the surface in the 3-FPEA and 4-FPEA systems but not in the PEA or 2-FPEA structures). Changing the solvent can have a dramatic affect on the grain structure and size. Methanol solutions were chosen because the resulting films consisted of reasonably sized and densely packed crystals, and yielded the best results for the field-effect transport measurements.

**Optical Properties.** Organic–inorganic hybrids of the form (RNH<sub>3</sub>)<sub>2</sub>MI<sub>4</sub> [M = Ge(II), Sn(II), or Pb(II)] are analogous to self-assembled quantum well structures, typically with smaller band gap inorganic sheets alternating with larger HOMO–LUMO gap organic layers. The hybrid perovskites exhibit sharp resonances in their room-temperature optical absorption spectra, arising from an exciton state associated with the

semiconducting inorganic sheets.<sup>21,37,38</sup> Because these excitons are associated with the band gap of the inorganic framework, the spectral positions of the transitions can be tailored by substituting different metal cations or halides within the inorganic sheets.<sup>21,38</sup> The strong binding energy of the excitons, which enables the optical features to be observed at room temperature, arises because of the two-dimensionality of the structure, along with the dielectric modulation among the organic and inorganic layers.<sup>39,40</sup> In addition to the sharp transition in the absorption spectra, the large exciton binding energy and oscillator strength lead to strong photoluminescence,<sup>21,37,38</sup> nonlinear optical effects,<sup>41,42</sup> and tunable polariton absorption.<sup>43</sup>

In the layered tin(II) iodide materials, the lowest exciton state arises from excitations between the valence

(37) Ishihara, T. In *Optical Properties of Low-Dimensional Materials*; Ogawa, T., Kanemitsu, Y., Eds.; World Scientific: Singapore, 1995; pp 288–339.

(38) Papavassiliou, G. C.; Koutselas, I. B. *Synth. Met.* **1995**, *71*, 1713.

(39) Hong, X.; Ishihara, T.; Nurmikko, A. V. *Phys. Rev. B* **1992**, *45*, 6961.

(40) Ishihara, T.; Takahashi, J.; Goto, T. *Solid State Commun.* **1989**, *69*, 933.

(41) Xu, C.; Kondo, T.; Sakakura, H.; Kumata, K.; Takahashi, Y.; Ito, R. *Solid State Commun.* **1991**, *79*, 245.

(42) Calabrese, J.; Jones, N. L.; Harlow, R. L.; Herron, N.; Thorn, D. L.; Wang, Y. *J. Am. Chem. Soc.* **1991**, *113*, 2328.

(43) Fujita, T.; Sato, Y.; Kuitani, T.; Ishihara, T. *Phys. Rev. B* **1998**, *57*, 12428.

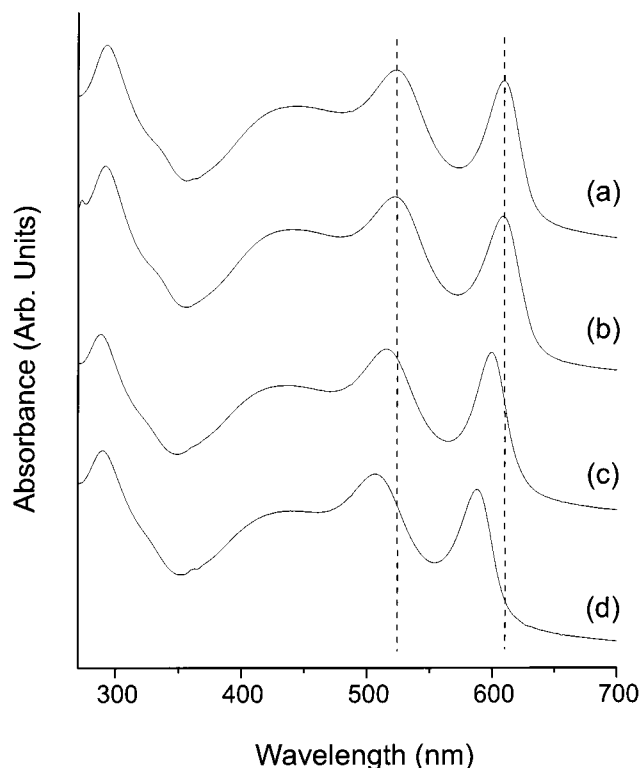


**Figure 9.** Room temperature UV–vis absorption spectra for spin coated thin films of (a)  $(\text{PEA})_2\text{SnI}_4$ , (b)  $(4\text{-FPEA})_2\text{SnI}_4$ , (c)  $(3\text{-FPEA})_2\text{SnI}_4$ , and (d)  $(2\text{-FPEA})_2\text{SnI}_4$  on quartz disks. The dashed lines are guides for the eye to highlight the shift in spectral feature position.

band, which consists of a hybridization of Sn(5s) and I(5p) states, and the conduction band, which derives primarily from Sn(5p) states.<sup>34</sup> In addition to tailoring the position of the optical features by making substitutions on the metal or halogen sites, control over the specific structure of the metal halide sheets through the appropriate choice of the organic cation should also provide a means of influencing the optical properties. In the case of the three fluorophenethylammonium-based hybrids, the most significant structural changes induced by the organic cation substitution include a progressive shift in the Sn–I–Sn angle from  $156.375(8)^\circ$  for the 4-FPEA system, to  $154.16(3)$  and  $153.28(3)^\circ$  (average) for the 3-FPEA and 2-FPEA analogues. The deviation in the Sn–I–Sn angle from  $180^\circ$  reflects the degree of relative rotation between neighboring tin(II) iodide octahedra. The Sn–I–Sn angle in  $(\text{PEA})_2\text{SnI}_4$  [ $156.48^\circ$  average] is most similar to that determined in the 4-FPEA system. The average Sn–I bond length is also larger in the 3-FPEA and 2-FPEA systems compared to that in the 4-FPEA and PEA compounds. Finally, the interaction between the fluorine and the inorganic sheet gets more pronounced in the 2-FPEA system. These structural differences should be reflected in the electronic properties of the materials.

A visual examination of 4-, 3-, and 2-fluorophenethylammonium tin(II) iodide crystals or powders indicates a progressive transition to lighter coloration as the fluorine is shifted from the 4 to the 2 position (i.e., the 4-FPEA compound is a dark red, whereas the 2-FPEA compound is a lighter red and the 3-FPEA system is intermediate in color). Figure 9 shows the room temperature absorption spectra for thin films of the three

fluorophenethylammonium-based systems, along with the corresponding PEA-based tin(II) iodide perovskite. Clearly evident in this data is the fact that the exciton state shifts to lower energy progressing from the 2-FPEA system (588 nm; 2.11 eV) to the 3-FPEA (599 nm; 2.07 eV) and 4-FPEA (609 nm; 2.04 eV) systems. A corresponding shift is noted for the band edge of the three systems. Note that the optical spectrum for  $(4\text{-FPEA})_2\text{SnI}_4$  is virtually indistinguishable from that for the PEA system. The exciton peak spectral position in  $(\text{PEA})_2\text{SnI}_4$  for the current study is in good agreement with previous reports.<sup>3,34</sup>

In the current  $(m\text{-FPEA})_2\text{SnI}_4$  films, the  $m = 4$  and  $m = 3$  systems have a very similar grain structure, whereas the  $m = 2$  films exhibit substantially smaller grain size (see Figure 8). It is doubtful, however, that these differences in grain structure substantially account for the observed shift in optical properties, because a noticeable shift in the color of the three materials is observed even in single crystals and ground powders of the compounds, consistent with the optical measurements on the films. Furthermore, the grain structures for the  $m = 3$  and  $m = 4$  materials are very similar, despite the shift in optical properties. The observed differences are therefore more likely primarily attributable to crystal structure changes induced by the organic cation substitutions. Interestingly, the trend in exciton band position correlates very well with the deviation of the Sn–I–Sn angle from  $180^\circ$  in the four compounds examined. Clearly, however, other structural distinctions (as mentioned above) are also important in determining the electronic structure of the materials.

**Thin-Film Field-Effect Transistors.** Organic electronic devices hold substantial promise for use in new technologies, especially those requiring large area coverage, mechanical flexibility, low-temperature processing, and low over-all cost.<sup>18,44</sup> Many of the same processing and cost advantages of the organic materials can be achieved with the self-assembling perovskite materials with, however, the possibility of higher mobility arising from the covalently/ionically bonded inorganic component of the structure.<sup>3</sup> In fact, early OITFTs based on the hybrid perovskite  $(\text{PEA})_2\text{SnI}_4$  provided saturation-regime mobilities in the range of  $0.6 \text{ cm}^2 \text{ V}^{-1} \text{ s}^{-1}$ ,<sup>6</sup> among the highest values reported for semiconductors processed from solution at ambient temperature. To test the impact of organic cation substitution on device performance for the tin(II) iodide based perovskites, the  $m$ -fluorophenethylammonium tin(II) iodide series ( $m = 2, 3, \text{ or } 4$ ) was used in TFT channels and compared with devices based on the corresponding PEA-based perovskite  $(\text{PEA})_2\text{SnI}_4$ .

A representative plot of drain current,  $I_D$ , versus source-drain voltage (source is always grounded),  $V_D$ , is shown in Figure 10 as a function of the applied gate voltage,  $V_G$ , for a  $(4\text{-FPEA})_2\text{SnI}_4$  channel in a bottom-contact TFT configuration (Figure 10, inset). The  $p$ -channel TFT operates in accumulation mode upon application of a negative bias to the gate electrode, as the concentration of holes contributing to  $I_D$  increases. Application of a positive gate bias depletes the channel

(44) Dimitrakopoulos, C. D.; Furman, B. K.; Graham, T.; Hegde, S.; Purushothaman, S. *Synth. Met.* **1998**, *92*, 47.

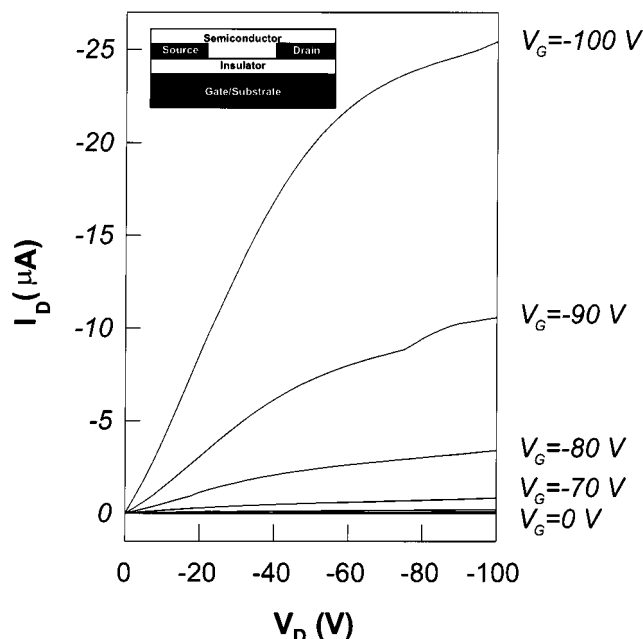


**Figure 10.** Drain current,  $I_D$ , versus source-drain voltage,  $V_D$ , as a function of the gate voltage,  $V_G$ , for a TFT with a spin-coated  $(4\text{-FPEA})_2\text{SnI}_4$  channel of length  $L = 15.4\ \mu\text{m}$  and width  $W = 1500\ \mu\text{m}$ . The gate dielectric is  $5000\ \text{\AA}\ \text{SiO}_2$ . Inset is a schematic of the device configuration.

of holes, turning the device off. At low  $V_D$ ,  $I_D$  increases approximately linearly with  $V_D$ , whereas at high  $V_D$ ,  $I_D$  saturates as the hole accumulation region in the channel is pinched off near the drain electrode.

The operation of the hybrid TFT is adequately modeled by standard field-effect transistor equations,<sup>45</sup> as is also the case for organic TFTs.<sup>44</sup> Plots of  $I_D$  and  $I_D^{1/2}$  versus  $V_G$  (Figure 11a) for a  $(4\text{-FPEA})_2\text{SnI}_4$  channel device yield a maximum field-effect mobility,  $\mu$ , in the saturation regime of  $0.48\ \text{cm}^2\ \text{V}^{-1}\ \text{s}^{-1}$ , with a threshold voltage  $V_T = -70\ \text{V}$  and an on-off ratio,  $I_{\text{on}}/I_{\text{off}}$ , of approximately  $10^5$ . The mobility values for the hybrid devices depend sensitively on surface preparation, contact type, and deposition conditions. Values of mobility between  $0.11$  and  $0.56\ \text{cm}^2\ \text{V}^{-1}\ \text{s}^{-1}$  have been typically noted for  $(4\text{-FPEA})_2\text{SnI}_4$  devices, similar to the figures previously reported for  $(\text{PEA})_2\text{SnI}_4$  channels.<sup>5,6</sup> Note that in contrast to the previously reported  $I_D$  versus  $V_G$  curves for  $(\text{PEA})_2\text{SnI}_4$ ,<sup>3,6</sup> only a very minor discontinuity is observed in the present  $I_D$  versus  $V_G$  plots. There is, however, an inflection (or foot) observed at low currents in the  $I_D$  curve, indicative of either a second channel for transport or a reservoir of carriers, which are released when the device is switched into depletion mode. This feature has generally been observed in the other hybrid systems described in this paper and may relate to transport through trap states.

The field-effect mobility of the  $(4\text{-FPEA})_2\text{SnI}_4$  TFT depends quite strongly on  $V_G$  (Figure 11b), as previously reported for  $(\text{PEA})_2\text{SnI}_4$ ,<sup>6</sup> organic<sup>18</sup> and amorphous silicon devices.<sup>46</sup> As described for the organic semiconductors,<sup>18</sup> increasing  $V_G$  leads to an increased number of accumulated charges available in the channel to fill localized traps. At higher  $V_G$ , the trap states are

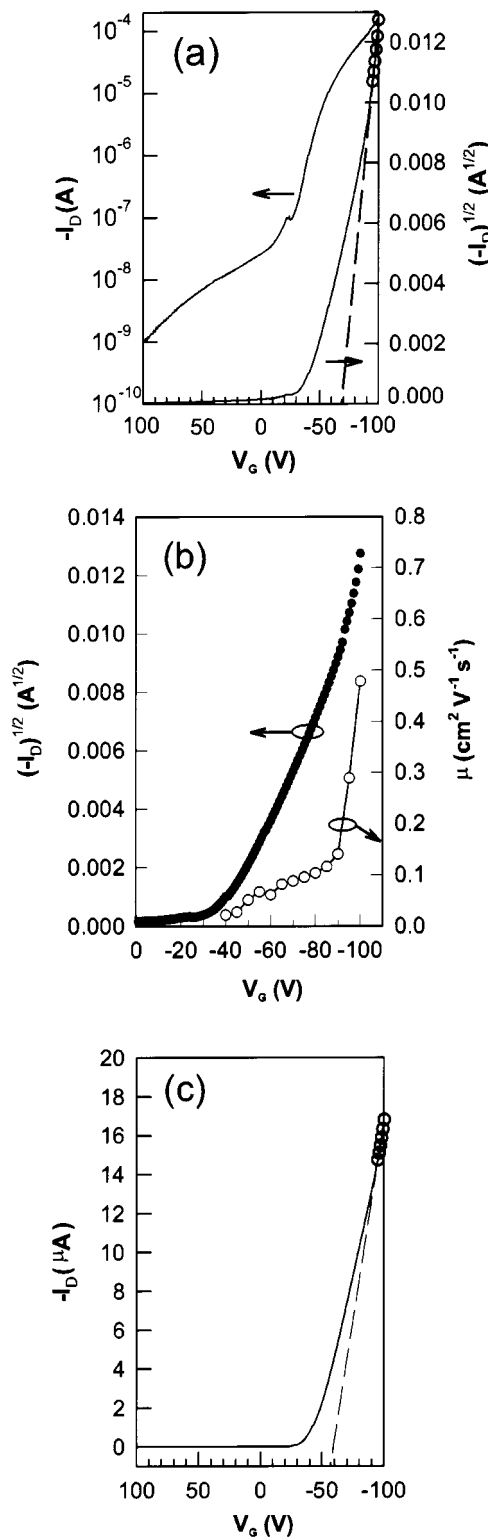


**Figure 11.** (a) Plots of  $I_D$  and  $I_D^{1/2}$  versus  $V_G$  at constant  $V_D = -100\ \text{V}$ , used to calculate current modulation,  $I_{\text{on}}/I_{\text{off}}$ , and field-effect mobility,  $\mu$ , for a TFT with a spin-coated  $(4\text{-FPEA})_2\text{SnI}_4$  channel of length  $L = 15.4\ \mu\text{m}$  and width  $W = 1500\ \mu\text{m}$ . The gate dielectric is  $5000\ \text{\AA}\ \text{SiO}_2$ . (b) Plot of mobility,  $\mu$ , versus  $V_G$  at  $V_D = -100\ \text{V}$  for the same device. The  $I_D^{1/2}$  versus  $V_G$  curve is replotted for comparison. (c) Corresponding linear-regime plot of  $I_D$  versus  $V_G$  at  $V_D = -10\ \text{V}$ .

therefore filled, enabling additional charges to move with the higher carrier mobilities characteristic of the delocalized band of the hybrid semiconductor. Thus, at high  $V_G$ , the calculated mobilities are largest, although

(45) Sze, S. M. *Physics of Semiconductor Devices*; Wiley: New York, 1981; p 442.

(46) Shur, M.; Hack, M.; Shaw, J. G. *J. Appl. Phys.* **1989**, *66*, 3371.

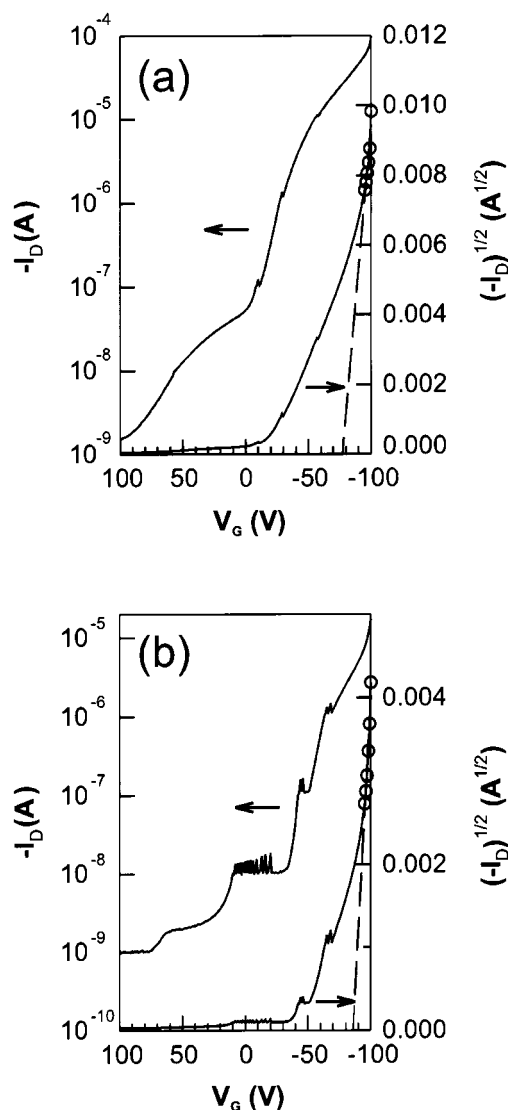


**Figure 12.** Plots of  $I_D$  and  $I_D^{1/2}$  versus  $V_G$  at constant  $V_D = -100$  V for TFTs with a spin-coated (a) (3-FPEA) $_2$ SnI $_4$  channel and (b) (2-FPEA) $_2$ SnI $_4$  channel, each of length  $L = 15.4$   $\mu\text{m}$  and width  $W = 1500$   $\mu\text{m}$ . The gate dielectric in each case is 5000  $\text{\AA}$  SiO $_2$ .

with a correspondingly higher threshold voltage (Figure 11a). Note that, as for the organic devices,<sup>18</sup> preliminary results for OITFTs made with higher dielectric constant gate insulators demonstrate operation at substantially lower voltages.<sup>47</sup> In comparison with the saturation-regime mobility, the linear-regime mobility (as calculated from the plot in Figure 11c) is  $0.06 \text{ cm}^2 \text{ V}^{-1} \text{ s}^{-1}$ , almost an order of magnitude lower than the saturation regime value. Such a large difference may be associated with a hysteresis in the device  $I$ – $V$  characteristics, which again can be related to trap states. Future studies should be targeted toward better understanding and perhaps eliminating these traps from the OITFT channels.

Figure 12 shows the  $I_D$  and  $I_D^{1/2}$  versus  $V_G$  curves for the same device geometry described above, except with the (4-FPEA) $_2$ SnI $_4$  channel replaced with a (3-FPEA) $_2$ SnI $_4$  (Figure 12a) and (2-FPEA) $_2$ SnI $_4$  (Figure 12b) channel.

The maximum saturation regime mobilities for the 3-FPEA and 2-FPEA devices shown in Figure 12 are  $0.51$  and  $0.24 \text{ cm}^2 \text{ V}^{-1} \text{ s}^{-1}$ , respectively, with similar gate voltage dependence to the mobility as for the 4-FPEA material. The threshold voltages,  $V_T$ , are  $-78$  and  $-85$  V, respectively. The corresponding linear-regime mobilities are  $0.06 \text{ cm}^2 \text{ V}^{-1} \text{ s}^{-1}$  for (3-FPEA) $_2$ SnI $_4$  and  $0.003 \text{ cm}^2 \text{ V}^{-1} \text{ s}^{-1}$  for (2-FPEA) $_2$ SnI $_4$ . The linear-regime mobility of the (3-FPEA) $_2$ SnI $_4$  device is about 1 order of magnitude lower than the saturation-regime mobility, whereas in the case of (2-FPEA) $_2$ SnI $_4$ , it is 2 orders of magnitude lower. This reduction of linear regime mobility relative to the saturation-regime value may be attributed to a larger concentration of traps, perhaps associated with the reduced grain size and increased importance of grain boundaries in the 2-FPEA material. In Figure 12a, there are two small discontinuities in the  $I_D$  versus  $V_G$  plots, whereas in Figure 12b, there are more prominent discontinuities, as has been observed in the (PEA) $_2$ SnI $_4$  materials.<sup>3,6</sup> If these discontinuities are again associated with trap populations, they further point to a higher trap density in the 2-FPEA materials. Note that many devices have been measured for each material and the values of the mobilities span a wide range depending upon device preparation conditions. For the 3-FPEA devices, the saturation-regime mobility has reached values as high as  $0.66 \text{ cm}^2 \text{ V}^{-1} \text{ s}^{-1}$ . Comparable devices made with the (PEA) $_2$ SnI $_4$  spin-coated films yielded saturation-regime mobilities as high as  $1.4 \text{ cm}^2 \text{ V}^{-1} \text{ s}^{-1}$ .

Although there is much variability in the hybrid TFT devices, the maximum currents achieved in devices for the three materials (prepared similarly), show an apparent dependence on which tin(II)-iodide-based derivative is chosen. For the (4-FPEA) $_2$ SnI $_4$  device shown in Figure 11a, the maximum drain current,  $I_D$ , achieved at  $V_G = -100$  V, is approximately  $160 \mu\text{A}$ . The corresponding currents in the 3-FPEA and 2-FPEA devices (Figure 12 parts a and b) are approximately  $100$  and  $20 \mu\text{A}$ , respectively. The trend in maximum current is consistent with the observation of a larger band gap for the (*m*-FPEA) $_2$ SnI $_4$  compounds as the fluorine shifts from  $m = 4$  to  $m = 2$ , as well as with the smaller grain size for the 2-FPEA system, and demonstrates the impact of the organic cation on device performance.

## Conclusion

Organic–inorganic perovskites provide a particularly flexible framework in which to tailor properties for potential applications and for the study of interesting physical properties. The fact that the hybrid perovskite films can be deposited using standard solution-based deposition techniques suggests that this materials set might find application in novel electronic devices, particularly those that take advantage of the ambient-temperature nature of the deposition (e.g., flexible devices made on plastic). In contrast to most metal halides, which are good insulators, the tin(II)-iodide-based perovskites exhibit semiconducting electronic character, with the potential for relatively high electrical mobility.<sup>7,8</sup> The electronic character of the tin(II) iodide framework can be tuned by making substitutions on the

(47) Dimitrakopoulos, C. D.; Mitzi, D. B.; Kosbar, L. Manuscript in preparation.

metal or halogen site.<sup>48,49</sup> In this study, we demonstrate that the organic cation can also be used to influence the electronic properties. This control is afforded by modifying the inorganic framework structure through steric interactions and hydrogen bonding between the organic cation and the inorganic sheets. In addition, the organic cation also influences the grain structure of the solution-processed film through either solubility effects or specific substrate–organic cation interactions.

The series (*m*-FPEA)<sub>2</sub>SnI<sub>4</sub> (*m* = 4, 3, or 2) provides a convenient system to examine the influence of the organic cation on the structural and electronic character of the hybrid systems. Shifting from *m* = 4 to *m* = 3 and *m* = 2 leads to more relative rotation between the neighboring SnI<sub>6</sub> octahedra within the inorganic sheets of the crystal structure, with the related (PEA)<sub>2</sub>SnI<sub>4</sub> structure being very similar to the *m* = 4 structure in this respect. The *m* = 4 and PEA systems also have a smaller average Sn–I bond length compared with the *m* = 3 and *m* = 2 systems, and there are differences in the degree of interaction between the fluorine atom and the tin(II) iodide octahedra for the three fluoro-substituted compounds. The progression in electronic structure is reflected in the optical properties, as the band edge and exciton states are found to shift to higher energy across the series *m* = 4 to *m* = 2 (the PEA system has an almost identical absorption spectrum to the *m* = 4 compound). The trend in optical properties presumably arises primarily from the changes in crystal structure, rather than from variations in grain structure, since the *m* = 3 and 4 films have very similar grain size and since a difference in optical properties is also clearly evident in ground powders and single crystals of the corresponding compounds. Field-effect mobilities for the three compounds in a TFT geometry are of the same order as that found in (PEA)<sub>2</sub>SnI<sub>4</sub>, with a strong dependence on substrate surface preparation, hybrid purity, and source/drain contact material. The peak current density in TFT devices shifts to lower values across the *m*-fluorophenethylammonium series, further demonstrating the influence of the organic cation on electronic properties.

(48) Weber, D. Z. *Naturforsch.* **1979**, *34b*, 939.

(49) Weber, D. Z. *Naturforsch.* **1978**, *33b*, 862.

Note that the ability to control the electronic properties of the hybrid multilayer structures by tuning the properties of the organic spacer layers, rather than by making substitutions on the metal or halogen sites, is important for several reasons. First, making atomic substitutions within the active metal halide sheets might negatively influence mobility values for the hybrids because disorder would be introduced into these layers. The organic chemistry of the modulation layer between the inorganic sheets can also be much more diverse than the simple substitutions that are possible within the inorganic layers. The inclusion of organic molecules with electron withdrawing or donating potential or with a wide range of steric influences, for example, can be expected to provide interesting possibilities for hybrid materials. There is also the interesting possibility of incorporating organic molecules with extended  $\pi$  systems, which may make it possible to induce electrical transport in the organic layer, as well as in the inorganic framework of the structure. Hybrid perovskites with an oligothiophene organic cation have already been demonstrated,<sup>13,14</sup> as well as those with anthracene- and naphthalene-based cations,<sup>50,51</sup> although the electrical properties of these systems have not been reported (in these current examples, the inorganic framework is insulating).

**Acknowledgment.** The authors would like to thank T. Graham for technical assistance and I. Koutselas, C. Kagan, and D. Williams for useful discussions regarding this work.

**Supporting Information Available:** Tables providing a full listing of experimental and crystallographic data for each of the three compounds (Table S1); atomic coordinates (Table S2) and anisotropic temperature factors (Table S3) for (4-FPEA)<sub>2</sub>SnI<sub>4</sub>; and atomic coordinates (Table S4/Table S7), anisotropic temperature factors (Table S5/Table S8), and a full listing of bond lengths and angles (Table S6/Table S9) for (3-FPEA)SnI<sub>4</sub>/(2-FPEA)<sub>2</sub>SnI<sub>4</sub> (PDF). This material is available free of charge via the Internet at <http://pubs.acs.org>.

CM010105G

(50) Braun, M.; Frey, W. Z. *Kristallogr.–New Cryst. Struct.* **1999**, *214*, 335.

(51) Braun, M.; Frey, W. Z. *Kristallogr.–New Cryst. Struct.* **1999**, *214*, 333.